Journal of Nuclear Materials 465 (2015) 390–399

Contents lists available at ScienceDirect

Journal of Nuclear Materials

journal homepage: www.elsevier.com/locate/jnucmat

Utilising DualEELS to probe the nanoscale mechanisms of the corrosion of Zircaloy-4 in 350 °C pressurised water

Kirsty J. Annand [a, *], Ian MacLaren [a], Mhairi Gass [b]

[a] Materials and Condensed Matter Physics, School of Physics and Astronomy, University of Glasgow, Glasgow G12 8QQ, UK
[b] AMEC Foster Wheeler, Clean Energy, Walton House, Birchwood Park, WA3 6GA, UK

ARTICLE INFO

Article history:
Received 5 February 2015
Received in revised form
8 June 2015
Accepted 9 June 2015
Available online 11 June 2015

ABSTRACT

Characterisation of materials utilised for fuel cladding in nuclear reactors prior to service is integral in order to understand corrosion mechanisms which would take place in reactor. Zircaloy-4 is one such material of choice for nuclear fuel containment in Pressurised Water Reactors (PWRs). In particular, the metal-oxide interface has been a predominant focus of previous research, however, due to the complex oxidation process of zirconium cladding, there is still no clear understanding of what is present at the interface. Using Scanning Transmission Electron Microscopy (STEM) and Dual Electron Energy Loss Spectroscopy (DualEELS), we have studied the corrosion of this material under conditions similar to those that could be encountered in service. It is shown that under all conditions, whether during faster oxidation in the early stages, slow growth just prior to the transition to a new growth regime, or in the faster growth that happens after this transition, the surface of the metal below the scale is loaded with oxygen up to around 33 at%. Approaching transition, in conditions of slow growth and slow oxygen supply, an additional metastable suboxide is apparent with a thickness of tens of nm. By studying changes in both chemical composition and dielectric function of the material at the oxide scale – metal interface with nanometre resolution, quantitative mapping could be achieved, clearly showing that this is a suboxide composition of ZrO and a Zr oxidation state close to +2.

1. Introduction

Zirconium alloys are used for fuel cladding elements and other structural components within several commercial designs of nuclear reactor due to their low thermal neutron cross section [1], high corrosion resistance [2], good mechanical properties, and favourable chemical stability in highly aggressive environments. Increasing the lifespan of a reactor's core components, without compromising the operational behaviour is of paramount importance to the nuclear industry for many reasons, including minimising waste production and the need for reprocessing. This will enable progress towards increased fuel burn-up and longer-lasting fuel elements. Consequently, water corrosion of the fuel containments has become a key factor in the limitation of the lifetime of fuel rods within nuclear reactors, and maintaining containment integrity under corrosion is critical to ensuring safe operation and preventing accidental release of radionuclides into the cooling water. It is therefore vital that any corrosion processes occurring are well understood, so that one can accurately predict the behaviour and lifespan of nuclear fuel rods.

By placing a zirconium alloy in contact with hot water (as for instance happens in pressurised water reactor or boiling water reactor designs) it reacts with the water resulting in oxidation of the surface and the liberation of hydrogen. The fate of the hydrogen is a large subject and will not be discussed in this paper, although some may diffuse into the metal and form hydrides. In the initial stages of corrosion a thin oxide layer is rapidly formed; however, this rate quickly decreases to follow the square or cube root of time [1–4]. This occurs up until an oxide layer of roughly 2 μm has formed on the surface of the metal. Following this, a kinetic transition occurs and the oxidation proceeds more rapidly again. This process may be repeated several times, until the oxide thickness grows almost linearly with time [2]. The cause of this rate change is not fully understood, although this is currently the focus of intense work in all countries using commercial nuclear power. One model is that faster routes for oxygen transport to the interface are created through pores and cracks perpendicular to the interface, which

* Corresponding author.
E-mail address: k.annand.1@research.gla.ac.uk (K.J. Annand).

http://dx.doi.org/10.1016/j.jnucmat.2015.06.022

allows for the transport of oxygen to the metal-oxide interface [5]. This repeated parabolic or cube root dependence of corrosion rate on time has been investigated in a number of studies.

Long term corrosion of a maximum of 10,507 days, allowed Hillner et al. [6] to gather approximately 14,500 data points to study the long term corrosion of Zircaloy, before and after irradiation. It was found that where the maximum corrosion scale thickness did not exceed 30 μm, there was a single linear post-transition rate constant found, whereas, at the highest temperatures where oxide film thicknesses exceeded 30 μm, two successive linear equations could be used to describe the data. The discrepancies in these findings were undoubtedly down to the fact that the corrosion thicknesses found at low temperatures were too thin to have reached the second transition point, and progress into the stage two kinetic region.

Motta et al. [7] studied oxides formed on three different alloys (Zircaloy-4, ZIRLO and Zr_2.5Nb) in both regular and lithiated water in order to model the growth of oxide layers formed on Zr alloys, and found that a regular periodicity in the corrosion process took place. This was repeatedly found using several different techniques (transmitted light optical microscopy, synchrotron radiation and TEM) which all corresponded well to the oxide transition thickness. They proposed a mechanism for oxide growth, which resulted in accumulation of stresses in the bulk oxide, and cracking to occur which resulted in the sample undergoing global transition.

This theory was validated when a new model to predict the oxidation kinetics of zirconium alloys in pressurised water reactors, named CORCY, was proposed by Bouineau et al. [8]. This model considered the effect of different environmental parameters on the corrosion of Zircaloy-4, such as temperature, irradiation, heat flux and hydriding and was based on a phenomenological approach where the oxidation kinetics were characterised by a cyclic repetition of a semi-parabolic law. It was found that the oxidation kinetics clearly showed a periodic behaviour, which was connected to the creation of periodic lateral cracks in the oxide layer and was observed both in out-of-pile loop and PWR tests. This strongly supports the theory that periodic corrosion kinetics occur both in and out of reactor. The corrosion kinetics of Zircaloy-4 could therefore be illustrated as a periodic repetition of a cubic law, more than likely due to the diffusion of oxygen into the zirconia layer, and the kinetic acceleration due to the transition. The authors explained the transition process as an accumulation of stresses in the oxide layer which ultimately reach a critical point, resulting in the creation of lateral cracking, releasing stress, and initiating the acceleration of the growth of the oxide layer.

In all these studies, the association between the transition and lateral cracking in the oxide layer depicts some interaction between the mechanical behaviour of the system, and its corrosion kinetics, but does not provide a clear understanding of the morphology of the metal:oxide interface during the corrosion process, at the nanometre level. Understanding why this transition behaviour happens is critical when modelling the rate of growth of oxide, and therefore to the lifetime prediction of Zr clads, and ultimately to the safety of nuclear power reactors. No model will be complete without a nanoscale understanding of what is going on during oxidation. Thus, it is essential that the oxide scale and the top layers of the metal are studied at nanometre resolution to reveal the detailed structural and chemical changes associated with diffusion of oxygen and the resulting oxidation of the metal. Whilst a number of techniques have been employed for this purpose, it is clear that various techniques within transmission electron microscopy (TEM) will be among the most versatile and informative for this purpose, although additional information can be added by techniques such as atom probe tomography.

Early experiments using an AEI EM microscope allowed Moseley et al. [9] to study the phases involved in the corrosion of Zircaloy-2 by hot water at 350 °C. By taking selected area diffraction patterns, it was deduced that a structure of Zr_3O was present within the sample. They also supposed that a sodium chloride type structure of ZrO was highly likely to exist in small quantities, the presence of which performed a transient role, as opposed to being a final oxidation product. The presence of a metastable oxygen-enriched band-like region at the metal-oxide interface was also suggested by Bossis et al. [10] and determined to have an ω-Zr hexagonal structure by analysis with TEM and energy-dispersive x-ray spectroscopy (EDX), but the exact composition of the phase was not postulated.

In order to determine a more detailed understanding of the morphology of any suboxide layers present, Yoshitaka et al. [11] used Auger Electron and X-ray photoelectron spectroscopy on samples of zirconium and Zircaloy-2. The comparison between corrosion in oxygen and water vapour at room temperature was made and three suboxides of Zr_2O, ZrO and Zr_2O_3 were found to occur on surfaces in both the oxygen and water vapour atmospheres. Early in the oxygen exposure (<5L(1L ≡ 10^{-6} Torr s)), and water vapour period (up to 30L), the primary suboxide found was Zr_2O. This suboxide was then found to undergo transformation from a +1 (Zr_2O) state, to a +4 (ZrO_2) state successively. Formation of a +2 state (ZrO) occurred after an exposure of 30L or higher in both environments.

Following this, Yilmazbayhan et al. [12] carried out cross sectional TEM investigations. They postulated from Energy Dispersive X-ray (EDX) spectroscopy that there may be evidence of a Zr_3O suboxide phase due to a gradual decrease in oxygen content from ~67 at.% in the bulk oxide to a level of ~29 at.% of oxygen solid solution in Zr. This was seen over a considerable distance from ~160 nm to ~560 nm in oxides formed on three different alloys: Zircaloy-4, Zr-2.5Nb and ZIRLO. More recently, Ni et al. [13] used electron energy loss spectroscopy (EELS) in order to quantify the oxygen content at the metal-oxide interface in a pre-transition ZIRLO sample after a range of pressurised water treatments. After calibration against a ZrO_2 powder standard, they were able to determine zirconium: oxygen ratios with good accuracy using a *k*-factor approach, at least for sample thicknesses less than 75 nm. Systematic differences in the local oxygen profile across the interface in different zirconium alloys were found. They concluded that in their pre-transition sample, a plateau region of around 130 nm wide in the oxygen concentration with a constant value of 50 ± 2 at.% between the ZrO_2 at 65 ± 1 at.% oxygen, and the metal, 31 ± 2 at.% oxygen was apparent, consistent with the presence of a suboxide phase above the Zr metal saturated with oxygen. They also noted that the interface region of a post-transition oxide showed no evidence of any intermediate suboxide.

By studying the microstructure of the metal-oxide interface region of Zircaloy-2 after autoclave corrosion testing, Tejland et al. [14] confirmed the presence of a sub-stoichiometric oxide layer, formed at the metal-oxide interface, which was found by EDX line scans across the metal:oxide interface to have an oxygen content of approximately 50 at. %. This suboxide was consistently found to have a thickness of around 200 nm. As expected, the oxygen concentration was found to be around 67 at% was found in the outermost part of the oxide, giving confidence in the EDX quantification. There was also found to be an oxygen concentration gradient into the metal in the region of 200 nm, from a level similar to the suboxide of about 30 at%, down to a few atomic percent. All tin from the metal matrix was found to be incorporated into the suboxide layer, and there was no evidence of any segregation to the metal:suboxide interface.

Subsequently, Ni et al. [15] performed TEM high angle annular dark field (HAADF) imaging of Zircaloy-4 samples and found no

evidence of a suboxide after 7 days of aqueous corrosion (15.3 mg dm^{-2}). After 114 days of corrosion, the same material produced a weight gain of 23.4 mg dm^{-2}. Atom probe tomography (APT) analysis highlighted an extremely well defined suboxide phase of a composition not dissimilar to ZrO occurring between the metal and the ZrO_2 oxide. TEM analysis of these pre-transition samples depicted a well defined intermediate phase after 34, 54 and 90 days of corrosion. In addition to the suboxide layers, oxygen-saturated (30 at% O) metal regions were found by both TEM and APT analysis beneath the interface in most of the samples studied. These were found to be thickest in the very late pre-transition samples and were significantly thinner in the post-transition samples.

Dong et al. [16] also studied the oxide scale morphology and oxide phases within three samples – pure Zr (crystal bar), Zircaloy-4, and Zr–0.4Fe–0.2Cr using atom probe tomography. Specimens were prepared from the oxide and oxide–metal interface regions from the three materials. A series of oxygen containing phases were found for all three alloys – a stable oxide ZrO_2 (in contact with water), the suboxide ZrO, a saturated solution of constant oxygen content at about 30% O – $Zr(O)_{sat}$ – and an undersaturated solid solution of O in Zr, denoted Zr(O), which had a decreasing oxygen content with distance from the oxide-metal interface. For Zircaloy-4 in particular, it was found that it follows a similar oxide sequence as that seen in crystal bar Zr, but with thicker intermediate layers of ZrO and $Zr(O)_{sat}$. They also observed the same effect as Ni et al. [15] whereby at low corrosion rates, the width of oxygen saturated zirconium was larger. Moreover, they noted that whilst the morphology of the oxide-suboxide interface was relatively uniform, the interface between the suboxide and the oxygen saturated metal exhibits 'semi-elliptical regions' of suboxide advancing into the oxygen saturated metal region.

Later studies by Tejland et al. [17] used TEM and HAADF contrast to confirm the existence of a wavy metal:oxide interface which undulates on a micrometer scale, but also has irregularities on a finer scale resulting in the formation of metal islands at wave crests. A suboxide layer was found to occur adjacent to the metal oxide interface, with a 45–55 at% oxygen composition. Again, the metal matrix was found to saturate with up to 32 at% oxygen, and the oxygen concentration profile into the metal matrix was found to be consistent with diffusion data for pure zirconium, although the oxygen diffusion profile was found to be wider under a metal hill, rather than at valleys.

All this presents strong experimental evidence that the ZrO phase is definitely seen in oxidation under conditions of slow oxide growth and thus restricted oxygen supply. There was however, until recently, little definite evidence about the structure of the phase since it is only ever metastable and is not easily formed in bulk. Early investigations by Schönberg [18] suggested a rock salt structure akin to α-TiO [19]. Puchala and Van der Ven [20] considered a number of possible structures using Density Functional Theory (DFT) modelling including the α-ZrO phase mentioned above and a δ-ZrO phase analogous to δ-TiO [21]. It was shown by atomistic modelling that the stable structure for ZrO is a modified form of the δ-TiO phase [20,22], which has been denoted δ′-ZrO. It was then confirmed by Nicholls et al. [22] using convergent beam electron diffraction that ZrO suboxides in both corroded Zircaloy-4 and ZIRLO samples do indeed exhibit the theoretically predicted hexagonal δ′-ZrO structure. Subsequently, Hu et al. [23] were able to consistently map the presence of δ′-ZrO at a metal-oxide interface using transmission electron backscatter diffraction (t-EBSD) and to correlate this to compositional measurements by EELS of a ZrO composition in corroded Zr-0.1%Nb alloys.

Whilst previous studies have used EELS to analyse the chemistry of the oxidation process, the quantification has been limited to a semi-quantitative *k*-factor approach that does not take proper account of multiple scattering within the material [13]. Moreover, it has not previously been possible to map larger areas of the oxide and metal, or to provide detailed correlated mapping between the electronic structure in the low loss and the chemical information from the high loss datasets. In order achieve these aims, it is necessary to use near-simultaneous recording of the low-loss and high-loss for all spectra, the so-called DualEELS approach [24]. Fast mapping, up to 1000 spectra per second, has now been introduced in commercially available spectrometers [25] and allows the mapping of hundreds of nm of sample at few nm resolution in a matter of minutes. The current paper applies DualEELS on a modern aberration-corrected STEM to the study of the evolution of the suboxide phase through the corrosion process, as well as revealing further details of its chemistry through the analysis of the details of the EEL spectra.

2. Experimental

2.1. Oxidation experiments

All samples were prepared by AMEC Clean Energy Europe. Samples were mechanically polished to remove surface scratches before being pickled in an HF solution to remove 50 μm of material from all surfaces. The samples were then exposed to pH 10 pressurised water at 180 bar and 350 °C with a hydrogen overpressure of 1.2 bar for various durations to simulate PWR in-reactor conditions [26,27]. Oxide thicknesses were average thicknesses, as inferred from weight gain measurements using the relationship 15 mg/dm^2 = 1 μm.

2.2. Sample preparation and scanning TEM

Samples were lifted out as cross sections through the oxide using a conventional focussed ion beam (FIB) lift out technique using a FEI Nova Nanolab instrument. Initial thinning was performed using 30 kV Gallium ions, after initial protection of the sample surface with electron beam and ion beam deposited platinum. Samples were then lifted out and attached to suitable copper support grids with platinum, and final thinning was performed using lower energy Ga beams down to 5 kV. Scanning transmission electron microscopy (STEM) and electron energy loss spectroscopy spectrum imaging (EELS-SI) using a probe corrected JEOL ARM200F (cold FEG) with a GIF Quantum ER electron energy loss spectrometer with DualEELS functionality. Typically, EELS acquisition was done with a probe with a semiconvergence angle of 29 mrad and a post-specimen lens setup that gave a spectrometer acceptance angle of 36 ± 0.4 mrad for EELS-SI. The Zr-$L_{2,3}$ edge data was recorded at an acceptance angle of 55.1 ± 0.9 mrad. Step sizes for EELS-SI were typically a few nm.

2.2.1. Limits on EELS resolution

In general, samples mapped were of the order of 100 nm thick, and multiple scattering was significant in all EELS data. Whilst this may have some impact on the spatial resolution of the EELS data, spreading of a beam not placed on a column of atoms along a low-index direction and subject to strong de-channelling is generally not that severe [28] and probably only limits the spatial resolution to a few nm at the worst (i.e. no worse than the map step size).

There was little limitation to resolution arising from the fundamentals of EELS excitation. Core loss edges like Zr-M or L and O–K are from inner electrons on the individual atoms and are, as such only excited by electrons within about 1 atomic radius of the atom of interest (i.e. ~ 2 A). The low loss plasmon region can be excited by Coulomb interactions at a larger distance [28],but in the

material with a reasonable concentrate of conduction band electrons, dielectric screening still reduces this effect significantly, keeping the effective resolution better than 1 nm, which is significantly below our resolution from beam spreading and our step size. Thus, the fundamental physics of EELS excitation will have a negligible effect on the spatial resolution of these measurements.

Of course, any overlaps of phases within the sample thickness are hard to resolve, although MLLS fitting of low loss can help here in identifying pixels containing two or more components (see below). Ultimately, the interface roughness imposes the most fundamental limit on the spatial resolution of these analyses.

2.3. Post-processing of electron energy loss spectroscopy data

Post-acquisition, datasets were processed using a sequence of steps, all performed within Gatan Digital Micrograph (version 2.3), in order to separate the real spectroscopic signals from artefacts and noise, and to quantify the resulting datasets. These processing steps are detailed below.

In some cases, there was a background beneath the low-loss part of the dataset that needed removal. This was performed as described recently by Bobynko et al. [29]. Any X-ray spikes in the datasets were then removed using a standard routine in Digital Micrograph. Low loss datasets were then cropped to remove the noisy areas to the left of the zero loss peak and above about 200 eV.

A Multivariate Statistical Analysis (MSA) [30] plug-in was utilised in order to perform Principal Component Analysis (PCA) on the datasets to separate the real signals from as many random noise components as possible and thereby produce low-noise spectra for mapping and quantitative evaluation.

Phase mapping was performed using a spectral fingerprinting approach using the Multiple Linear Least Squares (MLLS) approach using standard spectra extracted by summing spectra from a number of pixels from suitable phase-pure regions of the dataset. The MLLS fitting was performed in the range 5–60 eV to map phases based mainly on their dielectric response function. Clearly, in order for the MLLS fitting routine to provide a sensible fit to the data, low-loss spectra for all phases need to be included in the MLLS fit, otherwise spurious and misleading results are found. Notably, this meant that acceptable fits were only achieved for areas containing the ZrO suboxide if a low loss spectrum for this phase was included in the fit. It also meant that even low-loss spectra for the cracks in the oxide in the scan area had to be included as one of the components – these areas contain more surface material and thus have a strong surface plasmon contribution below 10 eV. All these low-loss spectra are shown in Fig. 1 below, and will be discussed in the following section. In this figure and in all the descriptions below, the following nomenclature is used for phases: Zr – alpha zirconium, ZrHy – zirconium hydride, Zr(O) – alpha zirconium containing diffused oxygen, ZrO – zirconium suboxide, and ZrO_2 – zirconium dioxide. In Fig. 1, the red dotted line (in web version) represents the energy (28 eV) where we would expect the Zr $N_{2,3}$ edge onset to occur. In accordance with expectations for such edges, the main peak of intensity is 10–15 eV later. Peak positions in low loss spectra were calculated using non-linear least squares fitting to Gaussian functions. For each phase, multiple measurements were taken over several datasets and an average was taken.

Quantitative mapping of the core-loss data was performed using a spectrum fitting approach, which explicitly accounts for multiple scattering [31], in a similar manner to earlier work [32–37]. The quantification of the data concentrated on the relative concentrations of Zr and O across the interface and was performed using the Zr-$M_{4,5}$ and O–K edges. Calculated partial cross sections for these edges were used. It was unnecessary to correct the data in any way and the outer oxide was quantified as ZrO_2, as expected.

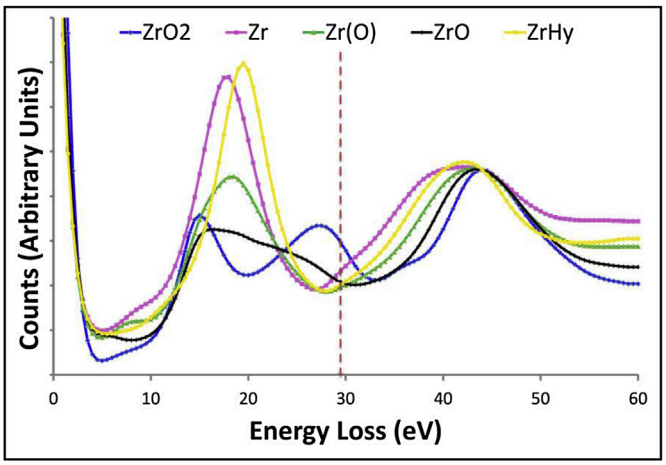

Fig. 1. Representative low loss spectra for each phase in the oxidised material, recorded for a Zircaloy-4 sample corroded in pressurised water reactor (PWR) conditions at 350 °C.

3. Results

3.1. Details of EELS spectra from the different phases

In order to understand the chemical maps presented in section 3.2, it is necessary to firstly examine the details of the EELS for each phase. Thus, we consider the low loss shape for each phase, the details of the O near-edge structure and how this changes in the transition from metal to oxide, and finally the details of the Zr $L_{2,3}$ edges and what this tells us about oxidation of zirconium.

3.1.1. Low loss shapes

In Fig. 1, everything should be compared to the two obvious end-members in the series. On the one hand, the alpha-Zr metal has just two peaks, a single plasmon peak at about 17.8 eV, in accordance with previous studies [22,38–41] and the delayed peak beyond the Zr $N_{2,3}$ edge at 28 eV. On the other hand, the ZrO_2 phase (blue (blue)) shows a three peaked spectral signature on the MLLS fit – two plasmon-like peaks, as in many oxides [22,38–41], one at 15.7 eV and the other at 27.3 eV, which are suppressed in intensity compared to the metal peak, followed by a rather delayed peak behind the Zr $N_{2,3}$ edge. Metal hydrides appear in the sample, both as a consequence of hydrogen uptake during corrosion, as well as during sample preparation. Their low loss signature is broadly similar to that of Zr metal, with a significant shift of the plasmon energy upwards to 19.6 eV. The oxygen diffused metal, the Zr(O), gives spectra of a similar shape to metallic Zr, although the plasmon peak is significantly damped, presumably due to the large amount of interstitial oxygen in the lattice. In view of the similarity of the plasmon shape to that in metallic zirconium, we can conclude that this region is likely to be metallic in nature, albeit with a higher resistivity than bulk metal. The ZrO spectrum shows a completely different fingerprint to what would be expected of a typical Zr signal. Instead, the primary plasmon peak is identified by a sharp onset followed by a gradually decreasing shoulder. This signal is clearly not a linear combination of the Zr and ZrO_2 phases, but rather, is a completely distinct signal in itself and is in very good agreement with the shapes calculated by Nicholls et al. [22], who calculated this as the sum of 3 different plasmon-like features centred at 13.9, 16.9 and 23.1 eV. This is clear evidence that this phase is no longer metallic in nature, and is an insulator or a semiconductor.

Measurements from the current work are compared with

previously measured or calculated values for these Plasmon peaks in Table 1. The reason for the slightly higher peak positions in this work as compared to previous work is uncertain, but the discrepancies are probably statistically significant as the precision should be of the order of 0.5 eV. We are quite certain that the calibration of the spectrometer used in this work was correct and linear, as this calibration was performed recently before these datasets were acquired. The fact that both the metal peak 1 and the oxide peak 1 are a little high does, however, point to calibration issues, either in this spectrometer or in previous EEL spectrometers used in older work, and this requires further investigation.

3.1.2. O electron energy loss near edge structure (ELNES)

Fig. 2 shows the O–K ELNES for three of the phases, ZrO_2, Zr(O) and ZrO. These have all been normalised to the same maximum height at the first peak. The ZrO_2 shape is consistent with expectations for this phase containing a clearly split peak consisting of a weaker p_1 peak at the front and a stronger p_2 component a few eV higher in energy [42–44]. In contrast to this, both Zr(O) and ZrO show a single peak midway between the p1 and p2 positions for ZrO_2. ZrO also shows a slight chemical shift, with respect to ZrO_2 with the edge onset energy about 1 eV later, which may indicate a reduction in the oxidation state and a reduced amount of charge transfer to the oxygen in this suboxide phase. The additional structure further behind the edge is more difficult to interpret without recourse to detailed multiple scattering simulations but it is notable that all three phases show characteristic shapes with significant differences in this region about 10 eV after the edge offset.

3.1.3. Zr $L_{2,3}$ ELNES

Fig. 3 shows the Zr-$L_{2,3}$ ELNES for three phases, Zr metal, ZrO and ZrO_2. Unsurprisingly, there is a significant increase in the L_3/L_2 ratio for ZrO_2 of 2.45 as compared with metallic Zr with 1.87, as is commonly seen for transition metal $L_{2,3}$ edges on oxidation as a result of the transfer of electrons from the *d* band to the oxygen. ZrO sits somewhere between these two extremes, with an L_3/L_2 ratio of 2.11. This shows clearly that the ZrO is an intermediate oxidation state between the 0 of the metal and the +4 of the ZrO_2, although it is not possible to directly relate the ratio to the oxidation state without calibrating this ratio to compounds of proven Zr oxidation state, as has previously been performed for Mn and Fe [45–49].

Additionally, there is a notable chemical shift of the onset of both edges on oxidation. At the L_3 edge, this is +2.5 eV for ZrO_2 as compared to Zr metal, as would be expected due to the increased binding energy for the remaining electrons in a Zr atom on the removal of some outer electrons. As expected, the ZrO lies midway between the two extremes with a shift of about +1 eV, suggesting an intermediate oxidation state. In summary, we conclude that the "ZrO" phase clearly has Zr in an oxidation state approximately midway between 0 and + 4, although further work with a standard would be required for definitive proof that this is +2.

Table 1
Peak positions in the low loss for the Zr and the ZrO_2, compared with previous published values.

	Metal (Zr)	Oxide (ZrO_2)	
	Peak 1 (eV)	Peak 1 (eV)	Peak 2 (eV)
This Work	17.8	15.7	27.3
P. Prieto et al. [41]	16.3	14.3	26
C. Palacio et al. [40]	15.9	13.9	27.6
K. O. Axelsson et al. [39]	16.2	13.8	27.3
J. Frandon et al. [38]	16.9	14.8	26
R. J. Nicholls et al. [22]	16.8	14.4	25.4

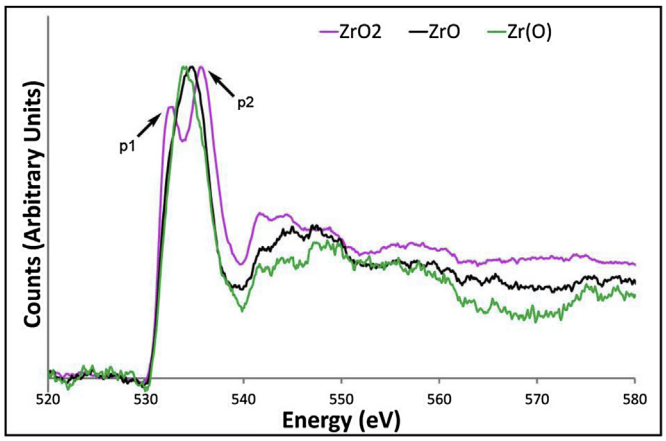

Fig. 2. A plot of the Oxygen K edges for the Zirconium Oxide (ZrO_2), oxygen saturated metal (Zr(O)) and the suboxide (ZrO) phases.

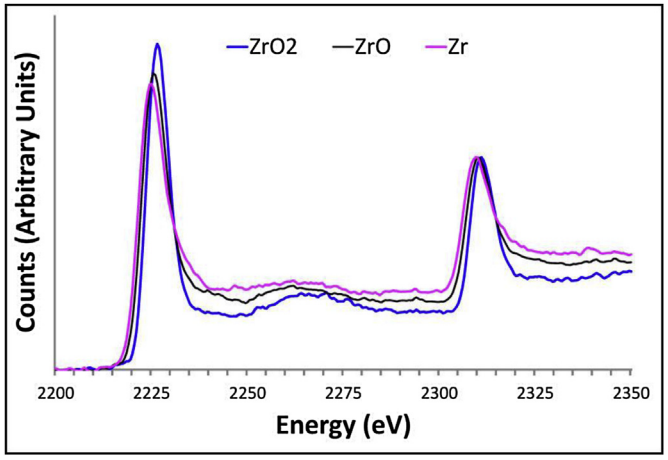

Fig. 3. Zr-$L_{2,3}$ ELNES for three phases: Zr metal, ZrO and ZrO_2.

3.2. Mapping of the interface through the corrosion process

Armed with a better understanding of the chemistry of the different phases from the EELS presented in section 3.1, we now show chemical mapping of 3 representative samples from different stages in the oxidation process. Firstly, we map a sample relatively early in the corrosion process, where the oxide growth was still fairly fast. Secondly, we map a sample almost at transition. Finally, we examine a sample that is clearly post-transition. In all cases, the data was collected in DualEELS mode and we compare the mapping of low loss shapes to identify different phases with a quantification of the Zr and O content from the core-loss spectra (accounting for multiple scattering).

3.2.1. Pre-transition

Fig. 4 shows maps of one area of oxide-metal interface in a sample corroded under accelerated pressurised water reactor (PWR) conditions at 350 °C in water to form an oxide of thickness 1.5 μm (prior to the transition to a rapid corrosion rate). It is immediately apparent in the O percentage map and the line trace that there is a relatively thick region of roughly 300 nm diffusion of oxygen into the metal matrix. This region is also clearly seen in the MLLS fit map to the low loss as the green phase (fitting the Zr(O) shape in Fig. 1). Quantifying the oxygen content in this region shows that it rises from almost zero in the pure metal to a plateau

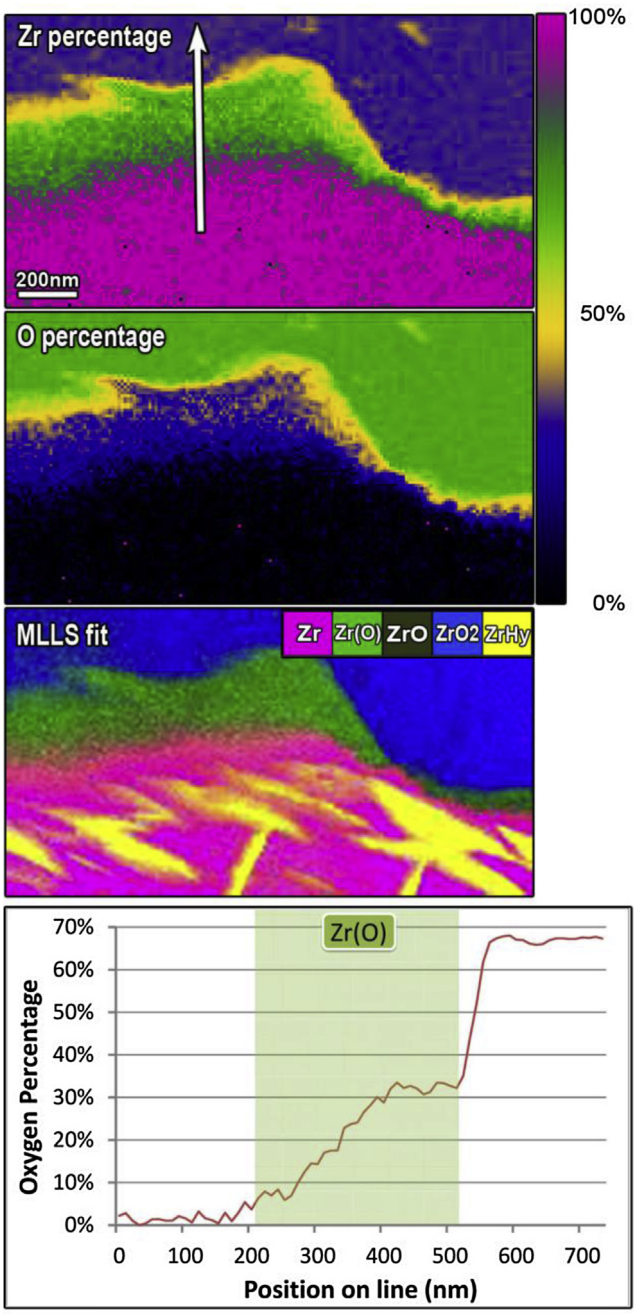

Fig. 4. EELS mapping of an oxide-metal interface in a pre-transition specimen. From top to bottom: Zr percentage composition map on a quantified colour scale; O percentage composition map on a quantified colour scale; multicolour composite image created from MLLS fitting of the low loss for each phase; line profile taken across the sample in the direction indicated by the arrow in the Zr percentage map, with an overlay box depicting the Zr(O) area. (For interpretation of the references to colour in this figure legend, the reader is referred to the web version of this article.)

region of around 30 at% oxygen, as exemplified by the plot. Whilst there is significant O-diffusion into the metal, there is absolutely no evidence for a ZrO suboxide phase in this sample – there is a very thin yellow line in the Zr and O percentage maps that corresponds to this composition (yellow is around 50% on the colour scale), but no distinct low loss shape for this phase is seen, even in the areas where the yellow area appears thicker. This suggests that the 50% regions are simply found as a consequence of interface roughness and the overlap of Zr(O) and ZrO_2 regions in the thickness of the specimen.

3.2.2. At transition

Fig. 5 shows maps of a sample corroded under the same conditions for longer until an oxide thickness of 2.17 μm was formed. From the corrosion data of numerous samples, it is known that this thickness is just prior to the transition point at which the corrosion rate increases again [5].

As for the pre-transition sample, there is a significant layer of oxygen diffused Zr, the so-called Zr(O) phase, as can be seen in green in the Zr percentage and the MLLS fit maps. This reaches thicknesses of 400–500 nm at points, and a peak composition just over 30 at% O. In contrast to the pre-transition sample, however, there is also a distinct suboxide phase between the Zr(O) and the ZrO_2. This shows up very clearly in both the Zr percentage and O percentage maps as yellow (~50%), and is depicted in the MLLS fit as black. This region is rather rough with sharply defined, almost saw-tooth shaped, boundaries to Zr(O) which is concurrent with findings by Ni et al. [15]. This suboxide region has thicknesses varying between just a few nm and 200 nm. In the particular case shown, there are additional areas of ZrO fully encased in the ZrO_2 below the crack.

3.2.3. Post-transition

Fig. 6 shows maps from a third sample, this time representative of the post transition phase of oxidation, with an oxide layer of around 2.85 μm in thickness. This sample exhibits an oxygen diffused metal region of around 150 nm, but it is clear that any suboxide layer is undetectable at this point in the oxidation process. As for Fig. 4, there is a very thin yellow line in the percentage maps, but this does not correspond to any ZrO low loss shape and is almost certainly just due to interface roughness in the thickness of the specimen, resulting in the overlap of ZrO_2 and Zr(O) areas.

4. Discussion

As has been shown previously, EELS is extremely well-suited to the analysis of the chemistry of Zr:ZrO_2 interfaces in oxidised Zr-base nuclear alloys [13,15,22]. Unfortunately, previous generations of spectrometers had limited speed readout and this restricted the area that could reasonably be analysed by EELS, and the majority of work was performed by simply taking line profiles through interfaces. The full complexity of the chemistry of the interfaces can only, however, be revealed in a two-dimensional map. With the advent of newer EEL spectrometers that can read out at up to 1000 spectra per second [25] it is now possible to map hundreds of nm of sample at a few nm resolution in a matter of minutes. This has been used in the present work to show both the phase distribution and detailed chemistry of these complex interfaces and to illustrate the changes that go on as the oxidation process advances.

Additionally, previous EELS studies have performed quantitative studies using just the core-loss spectra using a phenomenological *k*-factor approach corrected using the assumption that the outer oxide is ZrO_2 [13]. Clearly, this only works up to a point and does not properly account for the effects of specimen thickness and multiple scattering, and so the quantification results may not be entirely linear with concentration and may be slightly thickness dependent. It has been known for some time that the ideal approach is to remove the effects of multiple scattering from the quantification. This could be done in one of two ways: either the low loss spectrum is deconvolved from the core-loss spectrum [50] using the Fourier-log or Fourier-ratio methods, or the high loss spectrum is modelled as a forward convolution of a model spectrum and the low loss in an iterative procedure [32–36]. Both approaches have advantages and drawbacks, and a detailed discussion thereof is beyond the scope of this paper. In either case, mapping chemistry in a quantitative manner therefore requires a

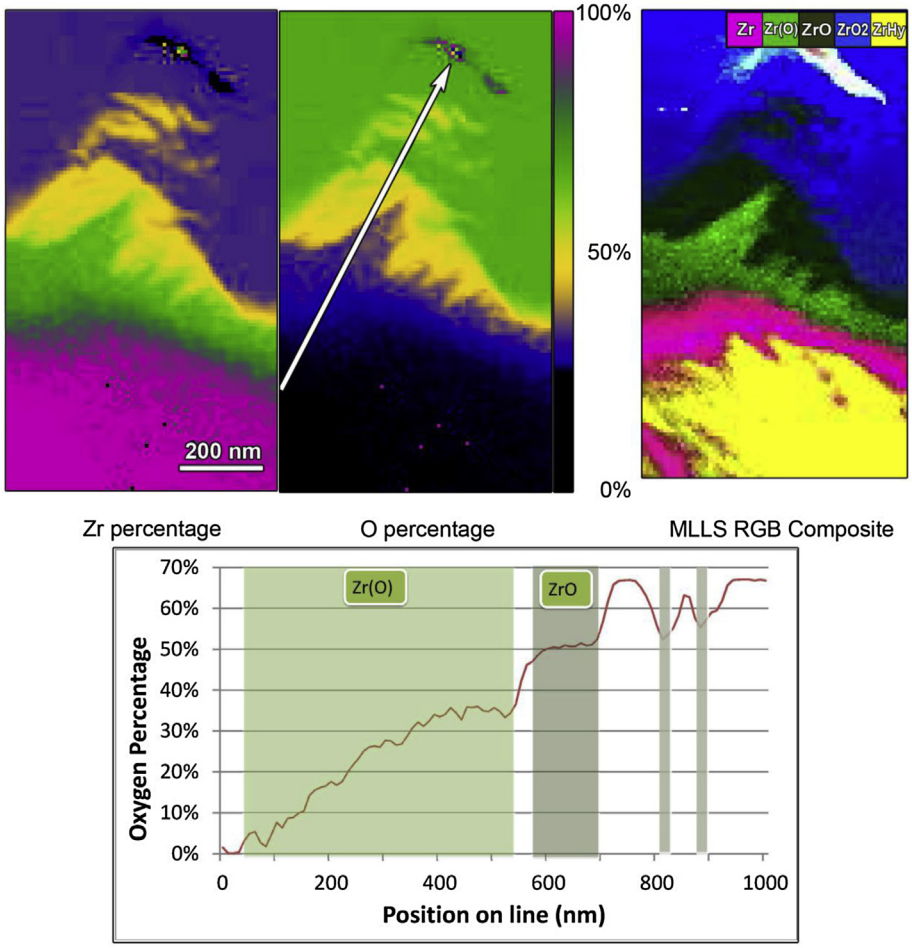

Fig. 5. EELS mapping of an oxide-metal interface in a specimen at transition. Along the top from left to right: Zr percentage composition map on a quantified colour scale; O percentage composition map on the same quantified colour scale; multicolour composite image created from MLLS fitting of the low loss for each phase. Bottom: line profile taken across the sample in the direction indicated by the arrow in the Zr percentage map, with overlay boxes depicting the Zr(O) and ZrO areas. (For interpretation of the references to colour in this figure legend, the reader is referred to the web version of this article.)

near-simultaneous, fast recording of the low-loss and the high-loss data. This capability has been developed in previous work at Glasgow on the development of the DualEELS concept [24]. The subsequent commercialisation of this into the latest generation of spectrometers and its combination with fast readout technology [25] has allowed the large area, high resolution DualEELS mapping that makes this quantitative visualisation of the chemistry possible in 2D. We have then chosen to use an EELS modelling approach to perform the quantification, as this worked well on the relatively thick specimens ($t/\lambda > 1$) used in this work, and was more noise tolerant than deconvolution.

An additional benefit of having the low loss datasets was that the plasmon and low loss shapes could also be mapped for each region. Since these are distinctive to each phase and act as a sensitive fingerprint of the local electronic structure (i.e. the real part of the dielectric function) then this is a powerful way of distinguishing similar phases, such as Zr metal from Zr hydride or Zr(O). The visualisation of these in multicolour maps using MLLS fitting therefore provides a useful counterpart to the quantitative Zr and O content maps from the core-loss spectroscopy. This has an additional advantage over the use of elemental quantification from core-loss EELS alone, that the overlap of two phases in the beam path due to the interface roughness will give a weighted average of the Zr:O ratio of the two phases, which is not unambiguously interpretable, whereas MLLS fitting fits this as a sum of the two phases with distinct low-loss shapes and is not confused by the overlap.

A further advantage of DualEELS for this kind of work is that these low loss spectral shapes can be analysed in detail for each mapped area. A new feature of this work is the clear and consistent reporting of a distinct plasmon shape for Zr(O), which appears at almost the same position as the plasmon for metallic Zr, but is significantly damped. It would suggest therefore that the incorporation of oxygen into Zr up to the solid solubility limit does not prevent the Zr(O) from behaving as a metal, but the damping of the metallic plasmon indicates a change in the resistivity of the metal. This presumably happens through impurity scattering by the interstitial oxygen atoms, and the high concentration of these oxygen atoms allows the impurity scattering to dominate the transport behaviour right to room temperature. In contrast to this, the ZrO shows a very clear 'shoulder' to the primary plasmon peak and this very spread peak is in good accordance with the experiments and simulations reported by Nicholls et al. [22].

A further unique feature of this study has been the possibility to measure the absolute energies and the relative chemical shifts of the Zr L_3 and L_2 edges with high reliability because of having the absolute reference of position of the zero loss peak for every data point. Consequently, we can clearly show that when going from metallic Zr to ZrO_2, a chemical shift of +2.5 eV is noticed at the L_3 edge. In the ZrO, this chemical shift was approximately +1 eV,

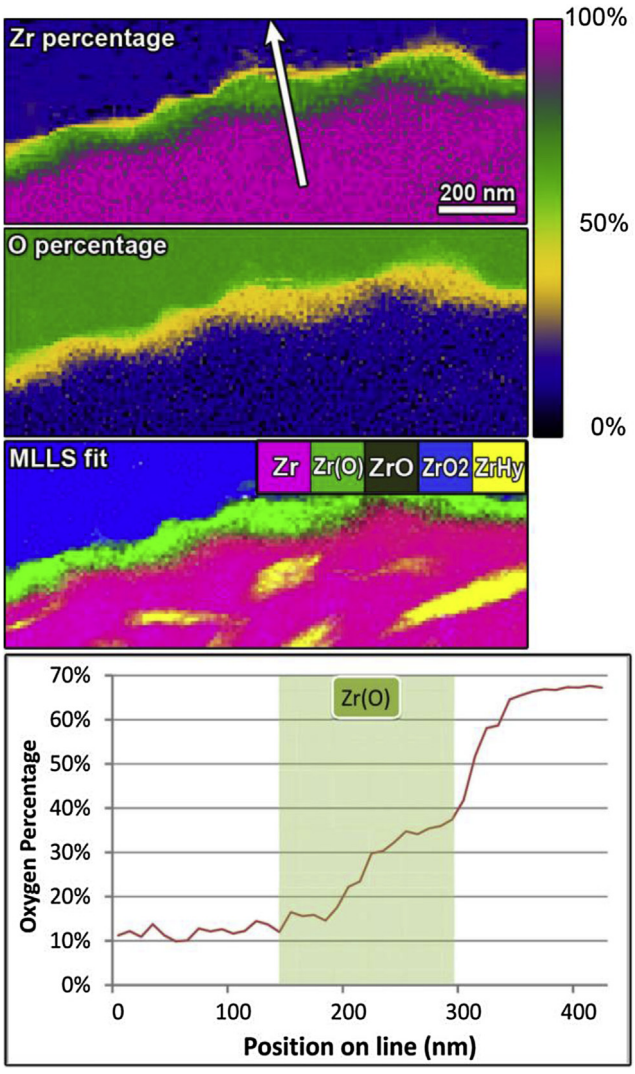

Fig. 6. EELS mapping of an oxide-metal interface in a post-transition specimen. From top to bottom: Zr percentage composition map on a quantified colour scale; O percentage composition map on a quantified colour scale; multicolour composite image created from MLLS fitting of the low loss for each phase; line profile taken across the sample in the direction indicated by the arrow in the Zr percentage map, with an overlay box depicting the Zr(O) area. (For interpretation of the references to colour in this figure legend, the reader is referred to the web version of this article.)

which would accord with it having an intermediate formal oxidation state between the 0 of Zr metal and the +4 of Zr in ZrO_2. This is consistent with work done on Zircaloy-2 by Yoshitaka et al. [11] who postulated a ZrO oxidation state of +2. Simultaneously, it was possible to examine the white line ratio of the L_3 and L_2 edges for these 3 phases in much the same way as has been performed for a range of first row transition metals in the past [45,46,48,49]. This showed that ZrO had a L_3/L_2 ratio of 2.11, which is midway between that for Zr^{4+} in ZrO_2 of 2.45 and that of Zr^0 in metallic Zr with 1.87. This follows a similar trend to that for iron oxidation in which the L_3/L_2 ratio increases with increasing oxidation state [46], rather than the trend seen for manganese in which the L_3/L_2 ratio decreases with increasing oxidation state [45,48,49]. In both of these studies, the relationship between the oxidation state and the white line ratio was non-linear. Consequently, there is no reason why the white line ratio of the Zr^{2+} state should be the arithmetic mean of those for Zr^0 and Zr^{4+}, which would be 2.16. Nevertheless, the fact that the measured white line ratio for ZrO is 2.11 certainly suggests that the oxidation state is likely to be close to +2. This could be confirmed by comparison with white line ratios from well-understood standards, as used in previous studies of first row transition elements [45,46,48,49]. More generally, this also suggests that the use of white lines ratios at the L_3 and L_2 edges could also be more generally used in EELS for the characterisation of the oxidation states of second row transition elements. Of course, it would also be possible to determine oxidation states of these elements by MLLS fitting between standard spectra, as was previously performed for Fe by Garvie and Buseck [47].

Moreover, analysis of the O electron energy loss near edge structure (ELNES) for the three phases – ZrO_2, Zr(O) and ZrO – allowed for the direct comparison of the shape of each of the oxygen K edges. As can be seen in Fig. 2, the ZrO O K near-edge structure has a somewhat similar shape to the O K structure of oxygen saturated Zr metal, albeit showing a shift in the ZrO edge onset energy about 1 eV later in comparison to Zr(O). This may indicate a reduction in the oxidation state and a reduced amount of charge transfer to the oxygen in this suboxide phase and highlights that they may have similar oxygen coordination. This is intuitive as the O positions in both oxygen saturated Zr and ZrO have similar bonding and coordination. Studies undertaken by Puchala et al. [20] confirm that as hexagonally close-packed Zr is able to dissolve unusually high amounts of oxygen into its interstitial octahedral sites, it has the ability to create a range of ordered suboxides up to a composition of ZrO. All of these contain oxygen in octahedral interstices. All were predicted to be metallic. Thus, the oxygen environments in ZrO and in the lower suboxides should be very similar and it is therefore not surprising that these have a very similar O–K ELNES, which was found to consist of a single unsplit peak just after the edge onset. It is likely that the subtle differences are due to the influence of other oxygen atoms on the Zr neighbours for ZrO, an effect that will be less prevalent for the lower suboxides. All this is radically different to ZrO_2, which showed a completely different ELNES, with a clearly defined split peak, consisting of a weaker p_1 peak at the front and a stronger p_2 component a few eV higher in energy [42–44]. Our observations are consistent with those of Ostanin et al. [42] for monoclinic (m) ZrO_2, which is already known to be the majority phase in our oxide scale [51].

With the benefit of the being able to map a few μm^2 of metal-oxide interface to show both phase composition and oxygen and zirconium content, it is now possible to discuss in more detail the chemical changes going on during the oxidation of Zircaloy-4 in superheated water. As shown in Fig. 4, in the pre-transition stage of corrosion after the initial fast growth phase, a certain degree of roughness develops on the oxide-metal interface. Parts of the interface (left of the Figure) lie deeper into the metal and suggest that oxidation has been happening faster at this point, whilst other parts (centre and right) show a slower growth of oxide into the metal. This correlates clearly with the thickness of oxygen-loaded zirconium. In the regions with fast growth of oxide, then there is little opportunity for further significant diffusion of oxygen into the metal ahead of the growth front and the Zr(O) layer is rather thin and much less than 100 nm. At other points where growth is slower, then the width of the Zr(O) layer is much larger, measuring hundreds of nm, and it would seem that when growth of oxide is slowed, the free oxygen available has time to diffuse long distances into the metal. The reasons for this roughening are not totally clear from this study, but it may be that local differences in the outer oxide scale are causing difference in the rate of oxygen transport that result in some regions growing quicker than others. These local variations in oxidation rate have also been seen by Ni et al. [15] in ZIRLO and by Tejland et al. [5,14] in samples of Zircaloy-2 who purport that this interface undulation exists in both the large scale (typically 20 μm) and on the small scale (typically around 1 μm),

and there is suggestion that this wavy interface is most probably a two-dimensional representation of a 3-dimensional "cauliflower" oxide structure. Bossis et al. [10] also confirmed using SEM on samples of Zircaloy-4, the occurrence of a wavy interface, identified as a succession of advanced and delayed portions of the oxidation front, distanced by up to 1 micron. These local deviations in the rate of oxidation have also been witnessed by Saillard et al. [52] when studying the development of stress-induced roughness during oxide scale growth on a metallic alloy for solid oxide fuel interconnects. At this early point in the corrosion process, however, there is no convincing evidence for the growth of any ZrO at this point in the corrosion, and oxygen supply to the interface is clearly sufficient to make direct conversion of Zr(O) to ZrO_2 the dominant process. This conclusion, whilst explaining the dataset presented here, is completely representative of a range of studies carried out on a number of pre-transition specimens.

As shown in Fig. 5, the interface roughness is further exaggerated in the sample at transition and additionally there is a now significant amount of ZrO at the interface. This roughness occurs both in the form of a bumpy metal oxide interface, but is also demonstrated by a rather jagged and well defined interface between the ZrO and the Zr(O). Such an effect has been seen previously by Ni et al. [15] (particularly in their Fig. 10), Bossis et al. [10], Tejland et al. [17] and has also been seen in other samples examined at Glasgow, both from this specific material and other near-transition specimens. This would suggest that the transition from oxygen loaded metal to ZrO is abrupt. Quite why this generates such saw-toothed structures, however, is an interesting question that requires further investigation. One particular feature of interest is that the largest amount of ZrO was found beneath a lateral crack at a particularly slow-growing part of the ZrO_2:Zr interface. Additionally some regions of ZrO were found stranded within the ZrO_2 beneath this crack. Finally, the Zr(O) area is relatively wide for most of the interface in this specimen. Quite why there is so much metastable ZrO and Zr(O) would tend to suggest one of two things. Either, the lateral crack is actually blocking the supply of oxygen to the region below it and thus stabilising the ZrO phase, as well as a particularly wide region of Zr(O) below this – which is entirely consistent with the recent work of Yardley et al. [53] who showed using ^{18}O tracer studies in SIMS that lateral cracks can block oxygen transport to the interface. Alternatively, rather than the cracks being the cause of slow oxidation, they could instead be the result thereof, since, due to very high tensile stresses perpendicular to the interface, cracks are formed above parts of the interface where the oxide front has not advanced so much [5,51,54]. Once the transition has taken place, the difference in the distribution of phases is remarkable. The metal-oxide interface is much flatter, no ZrO is found, and there is very little Zr(O). Again, this conclusion is based on examining many areas in the microscope, and not just one dataset. This transformation is consistent with a plentiful supply of oxygen to the interface through an interconnected network of cracks in the outer oxide resulting in fast oxidation and minimal formation of metastable phases. This is also consistent with the previous studies of Yardley et al. [53] and Ni et al. [15], that oxygen supply to the interface is very fast immediately after transition resulting in the fast growth of a dense oxide scale and a flat interface.

There is finally an interesting observation and question. In this work, it is found that the Zr(O) is wider where growth of oxide is slow and narrower where oxide growth is fast. This trend was not observed by Tejland et al. [14] for the oxidation of Zircaloy-2 tube, but this was only done for a small number of EDX line scans (rather than the larger area maps used in this work). However, similar observations to those in the present work have been made by Ni et al. [15] using combined EELS/STEM and APT analysis on samples of ZIRLO and Zircaloy-4 in order to study this oxygen-saturated (30 at% O) metal region. Evidence from diffraction patterns suggested that the Zr_3O phase is confined to this oxygen-saturated metal layer and after studies were performed on all samples, it was found that this layer was thickest in the (late) pre-transition samples and significantly thinner in the post-transition samples in much the same way as observed in our work.

According to Béranger and Lacombe [55], the diffusion profile only depends on the diffusion coefficient for oxygen in the metal, the time for diffusion and the oxygen concentration in the metal at the metal/oxide interface. The latter of these seems to be fixed at around 33% and the diffusion coefficient should also be fixed at any given growth temperature. However, the time for diffusion may well be much reduced if the oxide interface is growing rapidly, which may well explain this observation. Further work is needed on calculations to investigate this point in detail.

5. Conclusions

The evolution of the corrosion of Zircaloy-4 with time in 350 °C pressurised water conditions has been studied using FIB preparation of cross sections through the oxide scale followed by characterisation using DualEELS in the scanning transmission electron microscope. It has been shown that the low loss spectra provide a straightforward method for the mapping of phases in the complex interface region, and that the phases could be correlated with quantitative, thickness-corrected measurements of the Zr and O content from the core-loss spectra. The details of the low loss spectra for the ZrO phase match well to recent calculations using density functional theory. Zr L_3 and L_2 edges in EEL spectra show clear systematic changes in both chemical shift and white line ratio from Zr, through ZrO to ZrO_2 and suggest a formal Zr oxidation state in ZrO of +2, which is consistent with work by Yoshitaka [11], although further work with standards would be needed to prove this unambiguously. O K near-edge structure in ZrO suggests similar oxygen coordination to that in oxygen-diffused Zr metal, which makes sense since the O positions in both O-saturated Zr metal and ZrO are in octahedral interstices in a distorted hexagonal zirconium structure and are thus rather similarly bonded and coordinated.

The mapping of the corrosion process showed that in the earlier stages of growth, the metal-oxide interface starts to roughen with variable widths of oxygen-diffused metal, thicker where growth is slower and thinner where growth is faster. At this stage, little or no ZrO is found. Close to the transition where growth is very slow, significant thicknesses of ZrO are found, with a very rough saw-tooth interface to the underlying oxygen-diffused metal, especially where oxygen supply has been interrupted by lateral cracking about the metal-oxide interface. After transition, all the ZrO is lost, the interface roughness is minimal, and there is very little oxygen-diffused Zr, all of which accords well with existing models of increased oxygen supply after transition through the formation of interconnected porosity in the oxide scale, resulting in the rapid growth of a dense oxide.

Acknowledgements

IM and KJA are grateful to AMEC for funding this work and to AMEC and the EPSRC for the provision of a PhD studentship to KJA. This work would not have been possible without the provision of the MagTEM microscope facility by SUPA and the University of Glasgow. We are grateful to Dr Paul Thomas of Gatan UK Ltd. for helpful discussions on EELS quantification using DualEELS and the provision of experimental plug-ins for Digital Micrograph, together with prompt responses to technical questions and bug reports. IM is

also indebted to Prof. Alan J. Craven for his many helpful suggestions and discussions regarding EELS theory and data processing.

References

[1] S. Nakamura, H. Harada, S. Raman, P.E. Koehler, J. Nucl. Sci. Technol. 44 (2007) 21–28.
[2] B. Cox, J. Nucl. Mater. 336 (2005) 331–368.
[3] E.A. Gulbransen, K.F. Andrew, J. Electrochem. Soc. 105 (1958) 4–9.
[4] B. Cox, J. Nucl. Mater. 336 (2005) 331–368.
[5] P. Tejland, H. Andrén, J. Nucl. Mater. 430 (2012) 64–71.
[6] E. Hillner, D.G. Franklin, J.D. Smee, J. Nucl. Mater. 278 (2000) 334–345.
[7] A.T. Motta, A. Yilmazbayhan, R.J. Comstock, J. Partezana, G.P. Sabol, B. Lai, Z. Cai, J. ASTM Int. 2 (2005) 27.
[8] V. Bouineau, A. Ambard, G. Benier, D. Pecheur, J. Godlewski, L. Fayette, T. Duverneix, in: Proceedings of 15th International Symposium on Zr in the Nuclear Industry, Baltimore MD, USA, 2009, p. 24.
[9] P.T. Moseley, B. Hudson, J. Nucl. Mater. 99 (1981) 340–344.
[10] P. Bossis, G. Lelievre, P. Barberis, X. Iltis, F. Lefebvre, L. Thomas, M. Maguire, in: G.P. Sabol, G.D. Moan (Eds.), Zirconium in the Nuclear Industry: Twelfth International Symposium, ASTM International, 2000, pp. 918–945.
[11] N. Yoshitaka, A.R. Krauss, L. Yuping, D.M. Gruen, J. Nucl. Mater. 228 (1996) 346–353.
[12] A. Yilmazbayhan, E. Breval, A.T. Motta, R.J. Comstock, J. Nucl. Mater. 349 (2006) 265–281.
[13] N. Ni, S. Lozano-Perez, J. Sykes, C. Grovenor, Ultramicroscopy 111 (2011) 123–130.
[14] P. Tejland, M. Thuvander, H. Andrén, S. Ciurea, T. Andersson, M. Dahlbäck, L. Hallstadius, J. ASTM Int. 8 (2011) 24.
[15] N. Ni, D. Hudson, J. Wei, P. Wang, S. Lozano-Perez, G.D.W. Smith, J.M. Sykes, S.S. Yardley, K.L. Moore, S. Lyon, R. Cottis, M. Preuss, C.R.M. Grovenor, Acta Mater. 60 (2012) 7132–7149.
[16] Y. Dong, A.T. Motta, E.A. Marquis, J. Nucl. Mater. 442 (2013) 270–281.
[17] P. Tejland, H. Andrén, G. Sundell, M. Thuvander, B. Josefsson, L. Hallstadius, M. Ivermark, M. Dahlbäck, in: R. Comstock, P. Barberis (Eds.), Zirconium in the Nuclear Industry: 17th International Symposium, West Conshohocken, PA 2014, 2014, pp. 373–403. West Conshohocken PA.
[18] N. Schonberg, Acta Chem. Scand. 8 (1954) 627–629.
[19] E.S. Bumps, H.D. Kessler, M. Hansen, Trans. Am. Soc. Met. 45 (1953) 1008–1028.
[20] B. Puchala, A. Van der Ven, Phys. Rev. B 88 (2013) 094108.
[21] S. Andersson, Acta Chem. Scand. 13 (1959) 415–419.
[22] R.J. Nicholls, N. Ni, S. Lozano-Perez, A. London, D.W. McComb, P.D. Nellist, C.R.M. Grovenor, C.J. Pickard, J.R. Yates, Adv. Eng. Mater. 17 (2014) 211–215.
[23] J. Hu, A. Garner, N. Ni, A. Gholinia, R. Nicholls, S. Lozano-Perez, P. Frankel, M. Preuss, C. Grovenor, Micron 69 (2014) 35–42.
[24] J. Scott, P.J. Thomas, M. MacKenzie, S. McFadzean, J. Wilbrink, A.J. Craven, W.A.P. Nicholson, Ultramicroscopy 108 (2008) 1586–1594.
[25] A. Gubbens, M. Barfels, C. Trevor, R. Twesten, P. Mooney, P. Thomas, N. Menon, B. Kraus, C. Mao, B. McGinn, Ultramicroscopy 110 (2010) 962–970.
[26] T. Couvant, in: K.L. Murty (Ed.), Materials Ageing and Degradation in Light Water Reactors, Woodhead Publishing, 2013, pp. 70–80.
[27] M. Le Calvar, I. De Curières, in: D. Féron (Ed.), Nuclear Corrosion Science and Engineering, Woodhead Publishing, 2012, pp. 473–547.
[28] D.B. Williams, C.B. Carter, Transmission Electron Microscopy: a Textbook for Materials Science, Springer, US, 2009, p. 760.
[29] J. Bobynko, I. MacLaren, A.J. Craven, Ultramicroscopy 149 (2015) 9–20.
[30] G. Lucas, P. Burdet, M. Cantoni, C. Hébert, Micron 52–53 (2013) 49–56.
[31] P.J. Thomas, R.D. Twesten, Microsc. Microanal. 18 (2012) 968–969.
[32] H. Shuman, A.P. Somlyo, Ultramicroscopy 21 (1987) 23–32.
[33] R.D. Leapman, C.R. Swyt, Ultramicroscopy 26 (1988) 393–403.
[34] T. Manoubi, M. Tencé, M.G. Walls, C. Colliex, Microsc. Microanal. Microstruct. 1 (1990) 23–39.
[35] J. Verbeeck, S. Van Aert, Ultramicroscopy 101 (2004) 207–224.
[36] J. Verbeeck, S. Van Aert, G. Bertoni, Ultramicroscopy 106 (2006) 976–980.
[37] G. Bertoni, J. Verbeeck, Ultramicroscopy 108 (2008) 782–790.
[38] J. Frandon, B. Brousseau, F. Pradal, Phys. Stat. Sol. 98 (1980) 379–385.
[39] K.O. Axelsson, K.E. Keck, B. Kasemo, Surf. Sci. 164 (1985) 109–126.
[40] C. Palacio, J.M. Sanz, J.M. Martinez-Duart, Surf. Sci. 191 (1987) 385–394.
[41] P. Prieto, F. Yubero, E. Elizalde, J.M. Sanz, J. Vac. Sci. 14 (1996) 3181–3188.
[42] S. Ostanin, A.J. Craven, D.W. McComb, D. Vlachos, A. Alavi, M.W. Finnis, A. Paxton, Phys. Rev. B 62 (2000) 14728–14735.
[43] A. Shigeo, M. Shunsuke, M. Junya, S. Tsuyoshi, U. Yoshio, K. Kotaro, S. Hiroyasu, Mater. Trans. 45 (2004) 2951–2955.
[44] J.A. Aguiar, Q.M. Ramasse, M. Asta, N.D. Browning, J. Phys. Condens. Matter 24 (2012) 295503.
[45] Z.L. Wang, J.S. Yin, Y.D. Jiang, J. Zhang, Appl. Phys. Lett. 70 (1997) 3362–3364.
[46] P.A. Van Aken, B. Liebscher, V.J. Styrsa, Phys. Chem. Min. 25 (1998) 323–327.
[47] L.A.J. Garvie, P.R. Buseck, Nature 396 (1998) 667–670.
[48] Z.L. Wang, J.S. Yin, Y.D. Jiang, Micron 31 (2000) 571–580.
[49] Y.Q. Wang, I. Maclaren, X.F. Duan, Mater. Sci. Eng. A 318 (2001) 259–263.
[50] R.F. Egerton, Electron Energy-loss Spectroscopy in the Electron Microscope, Springer, New York, 2011.
[51] A. Garner, A. Gholinia, P. Frankel, M. Gass, I. MacLaren, M. Preuss, Acta Mater. 80 (2014) 159–171.
[52] A. Saillard, M. Cherkaoui, H. El Kadiri, Mater. Sci. Eng. 19 (2011) 015009.
[53] S.S. Yardley, K.L. Moore, N. Ni, J.F. Wei, S. Lyon, M. Preuss, S. Lozano-Perez, C.R.M. Grovenor, J. Nucl. Mater. 443 (2013) 436–443.
[54] E. Polatidis, P. Frankel, J. Wei, M. Klaus, R.J. Comstock, A. Ambard, S. Lyon, R.A. Cottis, M. Preuss, J. Nucl. Mater. 432 (2013) 102–112.
[55] G. Beranger, P. Lacombe, J. Nucl. Mater. 16 (1965) 190–207.